remote sensing

MDPI

Article

3D Geostrophy and Volume Transport in the Southern Ocean

María Isabel Vigo [1,*], David García-García [1], María Dolores Sempere [1] and Ben F. Chao [2]

[1] Department of Applied Mathematics, University of Alicante, E-03080 Alicante, Spain; d.garcia@ua.es (D.G.-G.); m.sempere@ua.es (M.D.S.)

[2] Institute of Earth Sciences, Academia Sinica, Taipei 11529, Taiwan, ROC; bfchao@earth.sinica.edu.tw

* Correspondence: vigo@ua.es

Received: 14 March 2018; Accepted: 3 May 2018; Published: 5 May 2018

Abstract: The 3D geostrophic currents and the associated volume transport (VT) can be estimated from the GOCE and Altimetry satellite data and in-situ temperature and salinity profiles measured by the Argo floats. We do so for the Southern Ocean between 20°S and 65°S with their time variability down to the depth of 1975 m (in 58 layers) over the 11-year period of 2004–2014. The results depict the Southern Ocean circulation where a zonal Antarctic Circumpolar Current (ACC) interacts with a meridional thermohaline circulation. The VT reproduces the polar front and the subantarctic front of the ACC, as well as the large scale and mesoscale currents in the Southern Ocean. Our estimates for the Agulhas current and the East Australia currents are also quantitatively comparable with results from other approaches in the literature based on in-situ data. For ACC, the estimated VT at the Drake Passage is 185 Sv for the norm of the time average VT, or 202 Sv for the mean of the norms of the monthly VT, which are larger than previous estimations (ranging from 134 to 175 Sv). The estimate is potentially reconciled when only the zonal transport is considered (181 Sv). The Drake Passage total VT appears to be quite stable during the studied period, unlike its (dominant) zonal and meridional components which show higher variability that mostly compensate each other. The spatially averaged ACC VT shows per 1° width in the main stream a mean value of 29.6 Sv or 35.8 Sv (depending on the method used), an annual signal with an amplitude of 0.33 ± 0.06 Sv that peaks in early April, with no significant semi-annual signals nor linear trend. Water transports of barotropic and baroclinic origin have been isolated in the VT series showing that 75% of transport is barotropic and the remaining 25% baroclinic, while the variability and annual signal in the ACC is fully barotropic.

Keywords: ocean geostrophy; water volume transport; satellite geodesy; space gravity; altimetry; Argo; Southern Ocean; ACC

1. Introduction

Physical forces acting on a body of water in the Navier-Stokes equation of motion include gravity, friction, Coriolis, and pressure gradient. In the oceans, dependent on the forces involved in the particular situation under consideration, different horizontal currents arise when wind stress is exerted on the sea surface. That balanced by the Coriolis force include the geostrophic and the Ekman flows. The geostrophic currents arise when the pressure gradient is balanced by the Coriolis force. It acts to the left (right) to the velocity direction in the southern (northern) hemisphere. The Ekman currents occur when the frictional force plays a significant role; its motion at the surface is 45° to the left (right) of the wind, while the total mass transport including all depths moves 90° to the left (right) on average. Ekman transport moves water mass to a side of the wind, which generates a pressure gradient that ultimately forms a geostrophic flow. Thus the two currents are not completely independent.

This study focuses on the geostrophic currents of the Southern Ocean. Historically, surface currents have been studied from ship drifter data [1], whereas the associated volume transport were inferred from in situ measurements of bottom [2], buoy or moored instruments [3], drifts and current meter records [4], hydrographic measurements [5], shipboard acoustic Doppler current profiler [6], and temperature (T) and salinity (S) climatological profiles [7]. In modern times, remote sensing instruments on board satellites opened new methodologies to observe currents. Wunsch and Gaposchkin [8] estimated the global geostrophic currents from hydrographic and altimetric sea level data, along with a modeled geoid. However, the necessary measurements were not accurate enough until decades later. The required quality of sea surface height (SSH) measurements was obtained in the early 1990s with the launch of the TOPEX/Poseidon (T/P) altimetric satellite [9]. The hydrographic measurements started to become continuous and globally monitored with the deployment of free-drifting profiling floats of the Argo project since 2000 [10]. In the meantime, the space gravity missions as GRACE and GOCE greatly improved the determination of the Earth's geoid [11]. Presently, the combined processing of these new datasets allows the estimation of not only the global ocean surface geostrophic currents but also the three-dimensional (3D) structures with depth.

Cadden et al. [12] obtained promising results by combining climatological T/S profiles and altimetric SSH measurements with a GRACE-derived geoid. Mulet et al. [13] studied the Atlantic Meridional Overturning Circulation by the Wunsch and Gaposchkin's method combining altimetric SSH, sea surface temperature, climatological Argo data, and a GRACE-based geoid. Kosempa and Chambers [14] obtained 3D geostrophic velocity fields combining satellite altimetry, a GRACE-based geoid and Argo T/S profiles. Their results were favorably compared to estimated currents at 1000 dbar based on Argo float trajectories. For the first time, geostrophic volume transport fields of the Southern Ocean have been obtained from their 3D geostrophy, where a significant correlation is evident between the average zonal transport over the entire Indian Ocean basin and the Antarctic Annual Oscillation at low frequencies. In this work we will use a GOCE-derived geoid, which is a notable advancement in precision and resolution over the GRACE based geoids .

The Antarctic Circumpolar Current (ACC) arises as the principal current when studying the geostrophic currents of the Southern Ocean. The mightiest and longest current not blocked by continents and connecting the Pacific, Atlantic and Indian oceans, it consists of two varying main fronts, which from north to south are the Subantarctic Front, and the Polar Front (Figure 1). Closer to Antarctica there is a third and weaker Southern Front. Adjacent to the coast there are two deep-reaching cyclonic gyres located at the Weddell and Ross Seas (Figure 1), and a third gyre between 80°E and 90°E of longitude (not shown in Figure 1). They are considered to bring ACC water near the cold continental coast to form deep waters [15]. It is worth noting that the ACC presents a net loss of heat to the atmosphere, that thermally isolates the cold Antarctic waters from the subtropical warm ones.

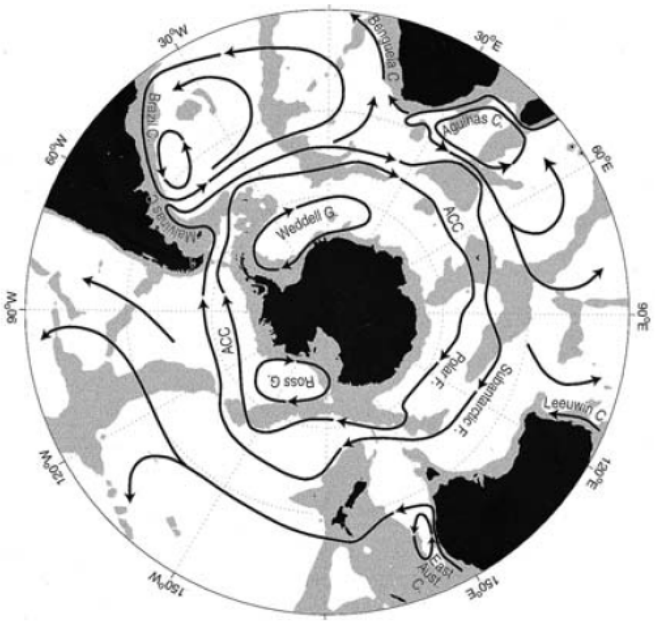

Figure 1. Schematic map of major currents in the southern hemisphere oceans south of 20°S, showing the two major cores of the Antarctic Circumpolar Current (ACC), the Subantarctic Front and the Polar Front. (F is short for front, C for current and G for gyre). Depths shallower than 3500 m are shaded. Reproduced with permission from Rintoul et al. [16].

Without global satellite coverage, the study of the ACC has been limited to the analysis of the currents at two passages. One is located south of Tasmania, where volume transports around 147 sverdrups (Sv = 10^6 m^3/s or 10^9 kg/s of flux) have been reported [17,18]. The second is the Drake Passage to the south of South America. The mean flow there varies between 134 to 140 Sv [2,5,19,20], while recent studies have considerably upped these estimates to 173–175 Sv [3,7].

In this study we shall calculate the 3D geostrophic currents and the associated volume transport (VT) using the SSH from a monthly merged solution from several altimetric missions, a geoid model from the GOCE mission, and the Argo monthly T/S profiles. We shall do so for the Southern Ocean between 20°S and 65°S at 58 depths from near surface to 1975 m depth for the 11-year period of 2004–2014.

2. Methodology

The geostrophic flow in the ocean can be estimated based on the combination of space and in situ data [8]. We do so using altimetric and gravity measurements from satellites, and in situ data from the Argo floats. To this end, we first define the Absolute Dynamic Topography (ADT) and the Relative Dynamic Topography (RDT) as follows:

$$ADT(x,y,t) = SSH(x,y,t) - N(x,y), \quad (1)$$

$$RDT(x,y,z,t) = \frac{1}{g(y)} \int_{P(z)}^{0} \frac{dP}{\rho(x,y,z,t)}, \quad (2)$$

where N represents a time-averaged geoid, x denotes the longitude, y the latitude, z depth, t time, g the latitude-dependent gravitational acceleration, $P(z)$ the pressure at depth z (in Pascal units), and ρ the density. We obtain the density from the ocean T, S, and pressure via the state Equation of Seawater from the Gibbs Seawater Oceanography Toolbox [21].

For the surface geostrophic currents, zonal speed (positive eastward) u_s and the meridional speed (positive northward) v_s follow from the geostrophic equation, i.e., the balance between the pressure gradient force and the Coriolis force at the surface:

$$\begin{aligned} u_s(x,y,t) &= -\frac{g(y)}{f}\frac{\partial ADT}{\partial y}(x,y,t), \\ v_s(x,y,t) &= \frac{g(y)}{f}\frac{\partial ADT}{\partial x}(x,y,t), \end{aligned} \tag{3}$$

where $f = 2\omega \sin y$ is the Coriolis parameter depending on ω, the angular rate of Earth's rotation. The surface geostrophic current provides the boundary value for the geostrophic current at any depth $z = z_i$ according to:

$$\begin{aligned} u_s(x,y,t) &= -\frac{g(y)}{f}\frac{\partial RDT}{\partial y}(x,y,z_i,t) + u(x,y,z_i,t), \\ v_s(x,y,t) &= \frac{g(y)}{f}\frac{\partial RDT}{\partial x}(x,y,z_i,t) + v(x,y,z_i,t). \end{aligned} \tag{4}$$

Substitution and expansion of Equations (3) and (4) allow one to calculate the geostrophic current at depth z_i from the geostrophic surface current and the spatial gradients of ADT and RDT (at depth z_i):

$$\begin{aligned} u(x,y,z_i,t) &= -\frac{g(y)}{f}\left(\frac{\partial ADT}{\partial y}(x,y,t) - \frac{\partial RDT}{\partial y}(x,y,z_i,t)\right), \\ v(x,y,z_i,t) &= \frac{g(y)}{f}\left(\frac{\partial ADT}{\partial x}(x,y,t) - \frac{\partial RDT}{\partial x}(x,y,z_i,t)\right). \end{aligned} \tag{5}$$

Estimating the geostrophic currents at several depths yields the three dimensional geostrophic flow, hereafter referred to as 3D geostrophy.

The volume of water transport at a cell of a regular grid from the surface to a depth D by the geostrophic flow can be estimated integrating vertically the 3D geostrophy from $z = -D$ to $z = 0$, and multiplying the result by the width of the cell perpendicular to the transport as follows:

$$\begin{aligned} VT_u(x,y,t) &= w_{NS} \cdot \int_{-D}^{0} u(x,y,z,t)dz, \\ VT_v(x,y,t) &= w_{EW}(y) \cdot \int_{-D}^{0} v(x,y,z,t)dz. \end{aligned} \tag{6}$$

where w_{NS} (w_{EW}) is the North-South (East-West) width of the grid cell. Note that in a regular grid w_{EW} depends on latitude y, unlike w_{NS}. Besides, both components of the VT depend on the depth of integration D. Units of volume transport are Sverdrups.

3. Data

3.1. Sea Surface Height

Sea level maps are provided by the CCI-Sea Level Project (http://www.esa-sealevel-cci.org) as a monthly merged solution from several altimetry satellites (Jason 1&2, Topex/Poseidon, Envisat, ERS1&2, GFO) for the time span 1993/01/01 to 2014/12/31, with a spatial resolution of 0.25 degrees. These maps are given as anomalies with respect to the DTU10-MSS mean sea surface where all

recommended geophysical and atmospheric corrections are applied. This version of the product is Version 1.1. The product can be found in "ESA Sea Level CCI project team (2016): ESA Sea Level Climate Change Initiative (Sea Level CCI): Time series of gridded Sea Level Anomalies (SLA). Centre for Environmental Data Analysis", downloaded in 06/2016. http://catalogue.ceda.ac.uk/uuid/682e9b455aae4f8fb2275580e8e21f1f (See [22] for further details).

3.2. Mean Sea Surface, Geoid, and Mean Dynamic Topography

A high-resolution mean sea surface model, DTU13MSS, computed by the Danish National Space Center [23] based on two decades of multi-mission satellite altimeters from nine different satellites has been used. By combining it with the geoid EIGEN-6C3, a high resolution global combined gravity field model based on the 4th release of the GOCE Direct Approach (see [24] for details), the DTU13MDT mean dynamic topography model was derived. Note that EIGEN-6C3 is a combined geoid model that also uses GRACE data and to reduce the applied filter it also assimilates surface gravity data based on satellite altimetry (mainly DTU10GRA). Andersen et al. [23] demonstrated that the Mean Dynamic Topography (MDT) DTU13MDT combined with DTU13MSS can be used to derive realistic geostrophic currents comparable to oceanographic derived MDT. Both data sets are available via ftp.space.dtu.dk/DTU13.

3.3. Temperature and Salinity Profiles from Argo Data

We use the Roemmich - Gilson Argo Climatology data [25] (data provided by SCRIPPS available at http://sio-argo.ucsd.edu/RG_Climatology.html, downloaded in April 2018). Data are $1^\circ \times 1^\circ$ regular monthly grids at 58 depths from near surface to 1975 m. They are estimated via weighted least-squares fit to the nearest 100 Argo-only T and S profiles. We take the time period 2004–2014 since at 2004 the number of Argo profiling floats reached 1000, and the southern limit of 65°S because that is the Argo spatial coverage limit.

3.4. Simulated Geostrophic Currents from ECCO Model

We shall compare our results against the output of the ECCO Model Version 4 Release 3 [26,27], for the overlapping period 2004–2014. This version of the model assimilates both in situ (T and S profiles, including Argo's), and satellite remote sensing measurements including sea surface height from altimetry missions, sea surface T and S, sea-ice concentration, and ocean bottom pressure from GRACE mission. Further details can be found at https://ecco.jpl.nasa.gov/products/all/. One of the outputs is the simulated surface currents as monthly maps with a spatial resolution of $0.5^\circ \times 0.5^\circ$, which are reduced to $1^\circ \times 1^\circ$ for comparison with our estimate. To obtain the gestrophic component of the ECCO Surface Currents we subtracted the Ekman component of the Surface Currents as obtained from GEKCO2 product [28]. The Ekman component was computed from remote-sensing altimeter and scatterometer data sets, and is distributed by the CERSAT as daily Ekman Surface Currents maps with a spatial resolution of $0.25^\circ \times 0.25^\circ$. Maps are reduced to monthly $1^\circ \times 1^\circ$ maps for comparison. In order to derive the RDT at different depths (see Equation (2)) we use ECCO T and S profiles at 37 depths down to 1975 m. From the RDT we derive the 3D geostrophic currents following the methodology of Section 2.

3.5. In-Situ Observations from Drifters

To validate the estimated surface geostrophic currents, their mean will be compared with in-situ measurements provided by drifting buoys. Here we use an annual climatology for the near-surface geostrophic currents from drifter buoys provided by the Global Drifter Program (www.aoml.noaa.gov, Version number: 3.1. Created on: 9 March 2018). A more detailed description of the data can be found in [29,30].

4. Results and Discussion

4.1. 3D Geostrophic Currents

The 3D geostrophic currents are computed according to Equation (5) at 58 depths from near surface to 1975 m depth for the period 2004–2014. We have computed the ADT and the velocities at the surface with a spacial resolution of 0.25°, whereas, for the RDT, the maximum spatial resolution is 1°. Thus, the 3D geostrophy is provided at 1° spatial resolution, but surface currents velocities have been computed at 0.25°. Note, that since the geostrophic velocity is based on the spatial gradient, its determinable speed at each point is affected by the spatial resolution of the data sets. The time-averaged zonal and meridional velocities at different depths are shown in Figures 2 and 3, while Figure 4 shows the mean of geostrophic current speed at the same depths. The latter is estimated as the Euclidean norm of the zonal and meridional components of the current. Note that the blank spots increase by depths due to the bathymetry. Furthermore, in Figure 3 we can discern approximately every three degrees meridional stripes that seem to be an artefact due to some of the processing of the data to produce the ADT. It likely comes from the assimilation of GRACE data in the used geoid, since GRACE has a polar orbit and meridional stripes are characteristic of unfiltered GRACE data (see e.g., [31]). Note that this noise is not observable in the geoid itself but comes out when it is combined with the SHH and we compute the partial derivatives to obtain the surface geostrophic currents. In any case, the noise only affects the meridional component, which in most of the cases is residual with respect to the zonal component in the studied region. This figures clearly illustrate geostrophic currents being strongest near the surface, whose strength decays with depth. The Subantartic and Polar fronts are clearly identified, showing a primary eastward component. The alternation of northward and southward components of the currents reveals the presence of eddies. Considering the 'ACC region' as contoured in Section 4.3 (see further details below), we obtain a mean (latitude weighted) speed at the region at different depths of 22.4 $\pm$ 0.2 cm/s (2.5 m), 19.7 $\pm$ 0.1 cm/s (500 m), 17 $\pm$ 0.1 cm/s (1000 m), 15.2 $\pm$ 0.1 cm/s (1500 m), and 14 $\pm$ 0.1 cm/s (1975 m). A mean decrease from the surface to 1975 m of 3.8 cm/s is observed, but in areas of maximum intensity this decrease reaches values over 25 cm/s, from which more than half (around 13 cm/s) takes place within the first 500 m depth, in both zonal and meridional components. The ACC also extends bellow the surface with decreasing strength, nevertheless it still reaches values as large as 30 cm/s at 1975 m, which is in good agreement with previous studies [32]. Note that besides ACC, the 3D geostrophy estimated here agrees well with the general current pattern of the Southern Ocean depicted in Figure 1, showing comparable current systems. For example, the Brazil-Malvinas Confluence region in the southwestern Atlantic basin can be observed with values ranging from 30 cm/s to 15 cm/s at 1975 m. The Agulhas Current, which is the warm shallow western boundary current of the southwest Indian Ocean, and the Benghela Current, which is the cold eastern boundary current of the southeast Atlantic Ocean, are very clear at all depths: a westward current can be seen from south Madagascar, becoming south-westward along the east coast of South Africa, and then moving eastward leaving the coast, while a west-northern current transports cold water from Antartica along the western South Africa coast. The northern part of the Ross Sea Gyre between 180°E and 120°W can also be recognized.

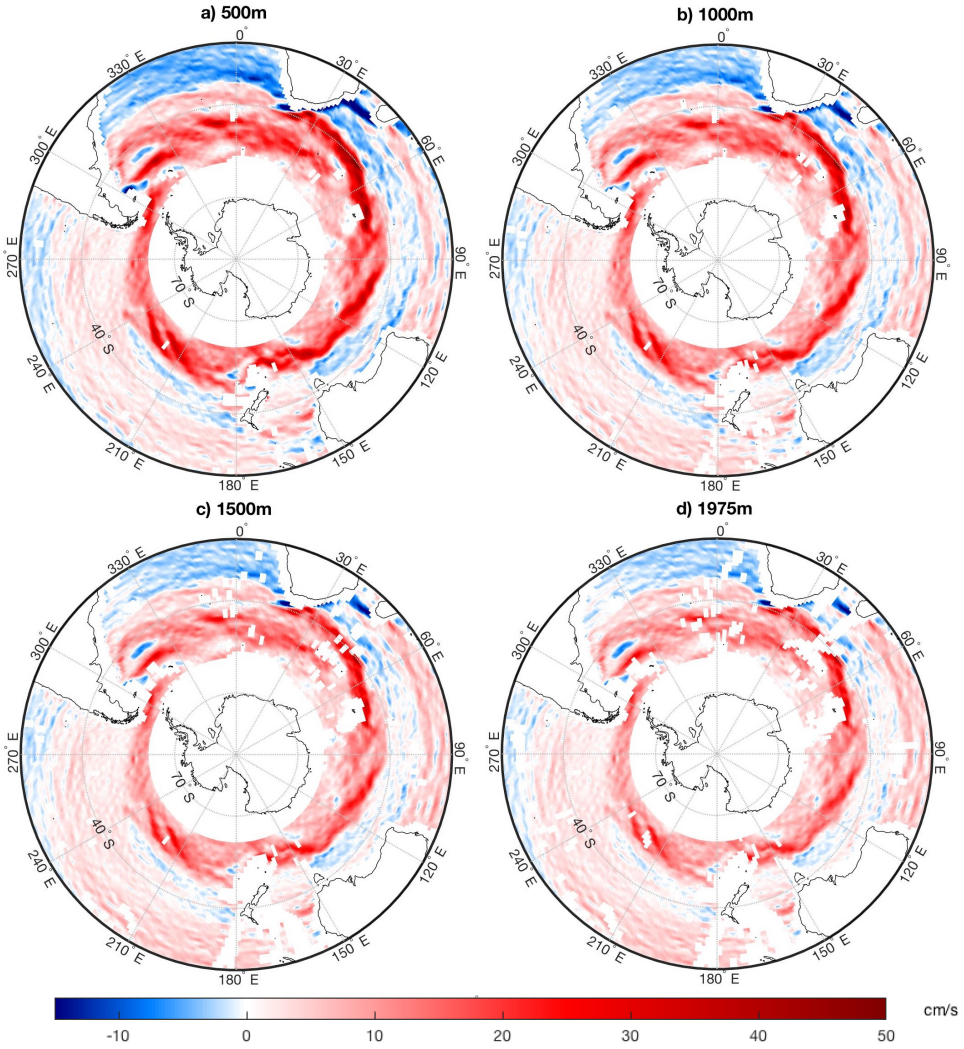

Figure 2. 2004–2014 Mean zonal geostrophic current at depths of: (**a**) 500 m, (**b**) 1000 m, (**c**) 1500 m, and (**d**) 1975 m. Positive (red) values represent eastward direction while negative (blue) westward. The zonal geostrophic currents reach values up to 60 cm/s (the color scale is saturated at 50 cm/s to better resolve the interrelation between different depths).

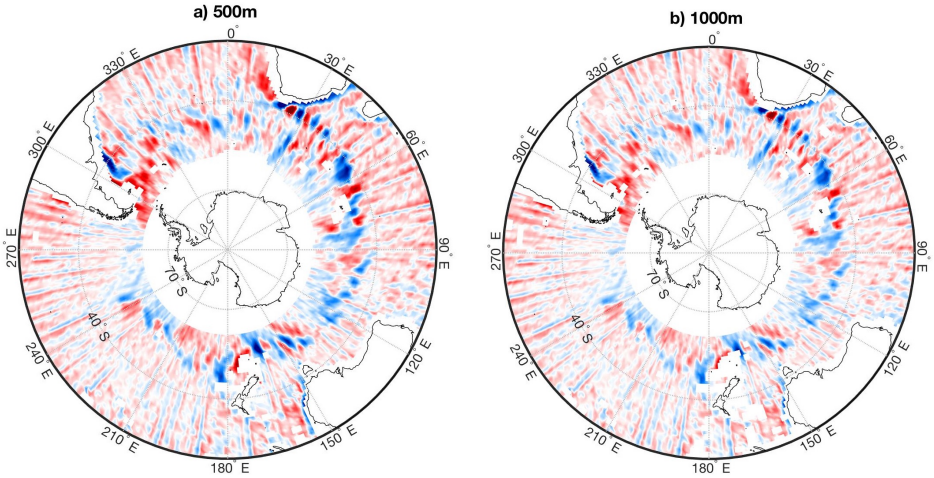

Figure 3. *Cont.*

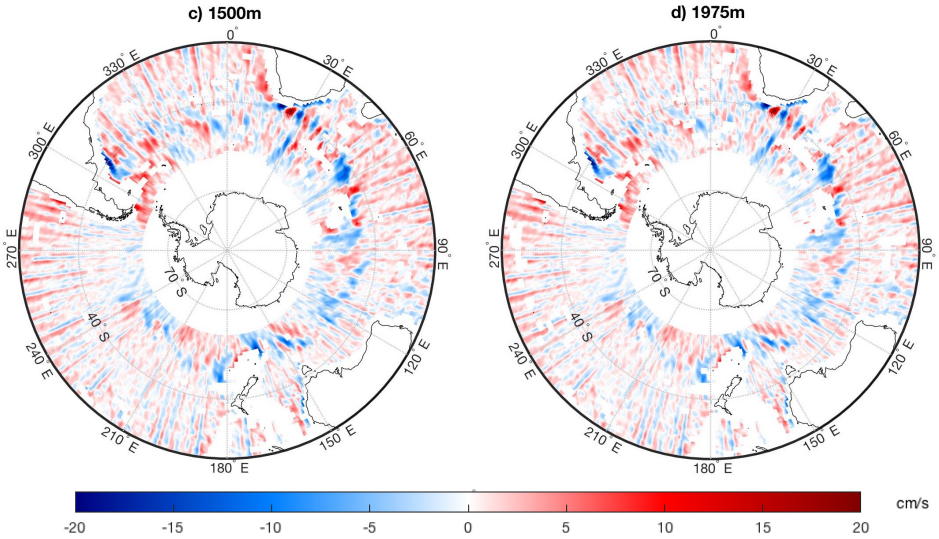

Figure 3. Same as Figure 2, but for the mean meridional Geostrophic current (color saturated at 20 cm/s).

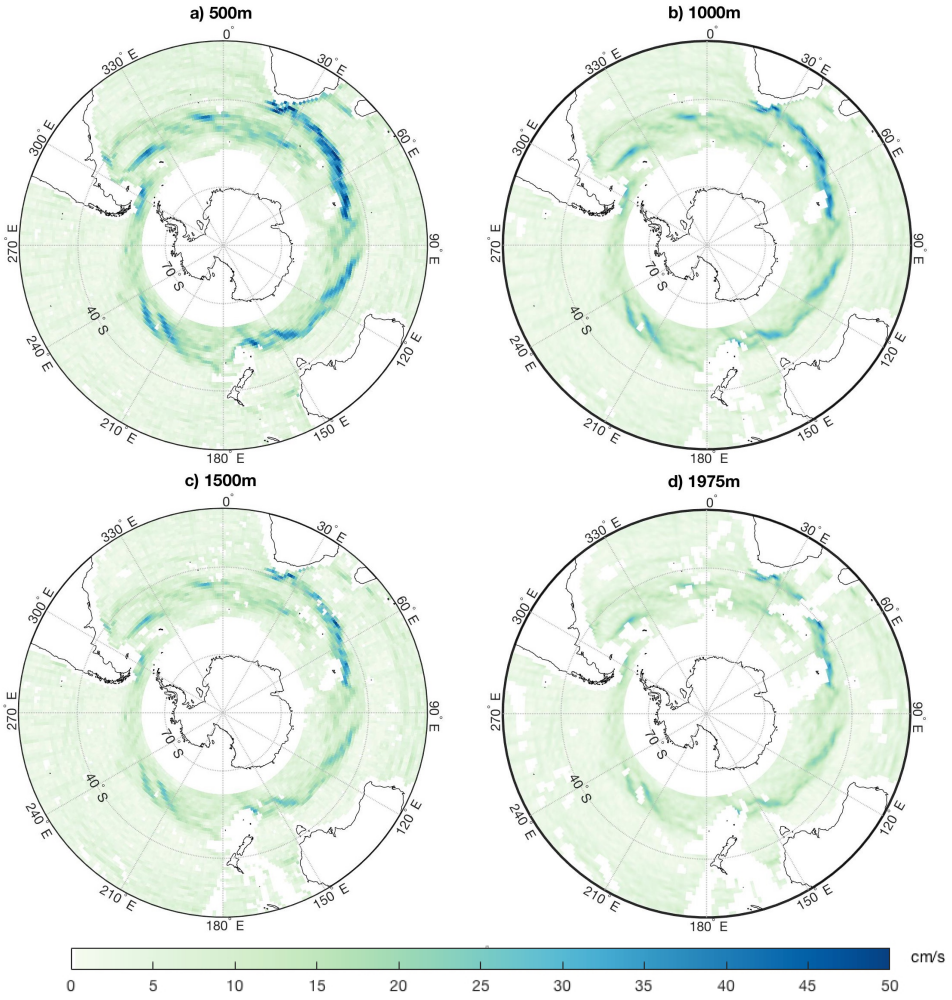

Figure 4. Same as Figure 2, but for the mean speed of the geostrophic current (color saturated at 65 cm/s).

4.2. Comparison with Simulated ECCO geoStrophic Currents and In-Situ Surface Currents Observations

We compare the 3D geostrophic currents derived from GOCE, altimetry, and Argo data for the region [65°S, 20°S] with the 3D Geostrophic currents from the ocean circulation model ECCO that assimilates in situ and satellite measurements (see Section 3.4). Note that, unlike ECCO, in this study we use a GOCE geoid which is independent from altimetry. For validation purposes, we also compare the two products with in situ observations derived from satellite-tracked surface drifting buoy observations [29] from which we remove the Eckam component in the same way as before (see Section 3.4). We will limit our validation to mean surface currents as only the time averaged velocities are available although the drifters currents uses data for the period 1979–2015.

Figure 5 shows the mean speed of the surface geostrophic currents from the three data sets: this study (GOCE and altimetry based), ECCO products, and Drifters. Our results and drifters show a remarkable good agreement whereas the ECCO value over the Southern Ocean presents much lower speeds (around 50% lower, note the different ranges of the color bar for Figure 5b). Considering the complex representation of the velocities $u + iv$, where u and v are the zonal and meridional components, we can obtain the complex correlation coefficient as described by Kundu [33] whose magnitude gives the overall measure of correlation and whose phase gives the average relative displacement or veering between the two velocity maps. For the velocities from this study and the drifters, the complex correlation coefficient is 0.78 with a mean angular offset of veering of 3°. While for the surface currents from ECCO and drifters, the complex correlation coefficient is slightly lower, at 0.69, though with a smaller relative shift of 0.9°, but notice that the angular offset of veering is more significant the higher the correlation is. Quantitatively our study suggests that the ECCO based approach significantly under-estimates the current variabilities while our approach produces a more realistic estimate closer to the direct drifter observations at least for the mean values. The two indirect methods use similar altimetric data, thus the improvement in our study illustrates the utility of an independent GOCE-derived geoid.

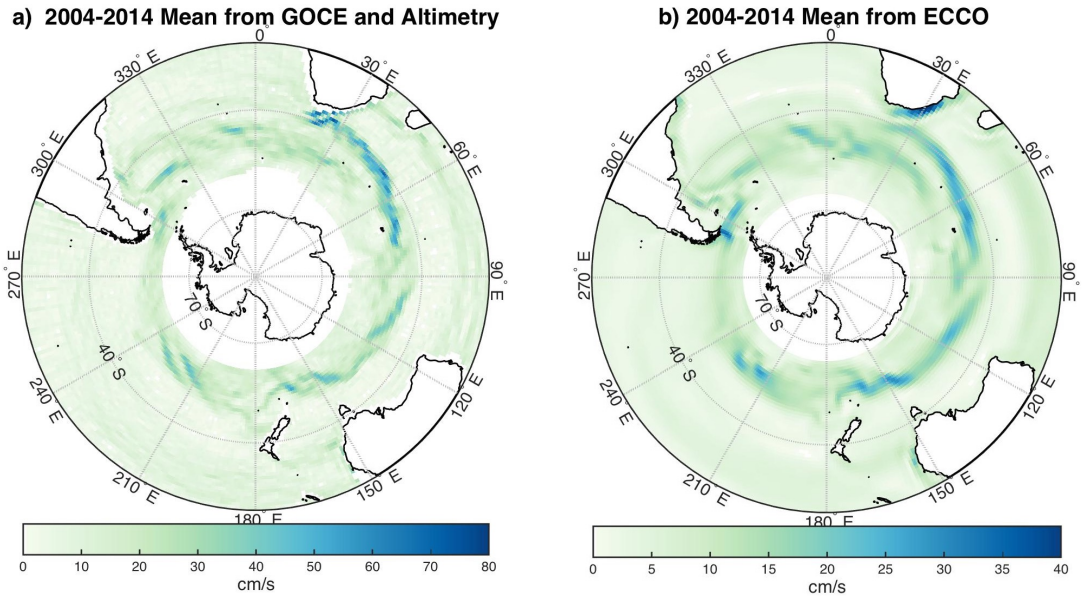

Figure 5. *Cont.*

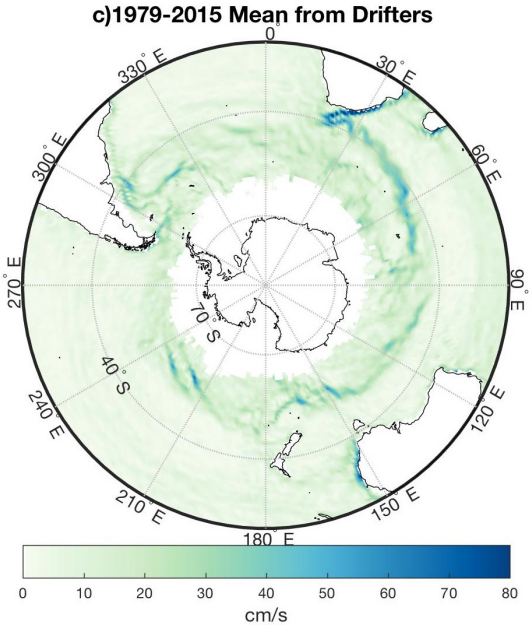

Figure 5. Mean surface geostrophic currents from (**a**) this study (GOCE and altimetry based), (**b**) ECCO, and (**c**) drifters. Note the different ranges of the color bar.

Figure 6 shows the mean speed variations from surface down to 1975 m depth for the 3D geostrophic currents from this study (GOCE, Altimetry, and Argo based), compared to those from ECCO products. Again the patterns are quite similar, but with lower intensities in the ECCO about 30%; the latter produces a lower intensity variation also by depths. Figure 6a also shows higher values in certain regions of the ACC, particularly south of Africa. Note that these variations with depth with respect to the surface depend on the RDT and not on the reference surface current.

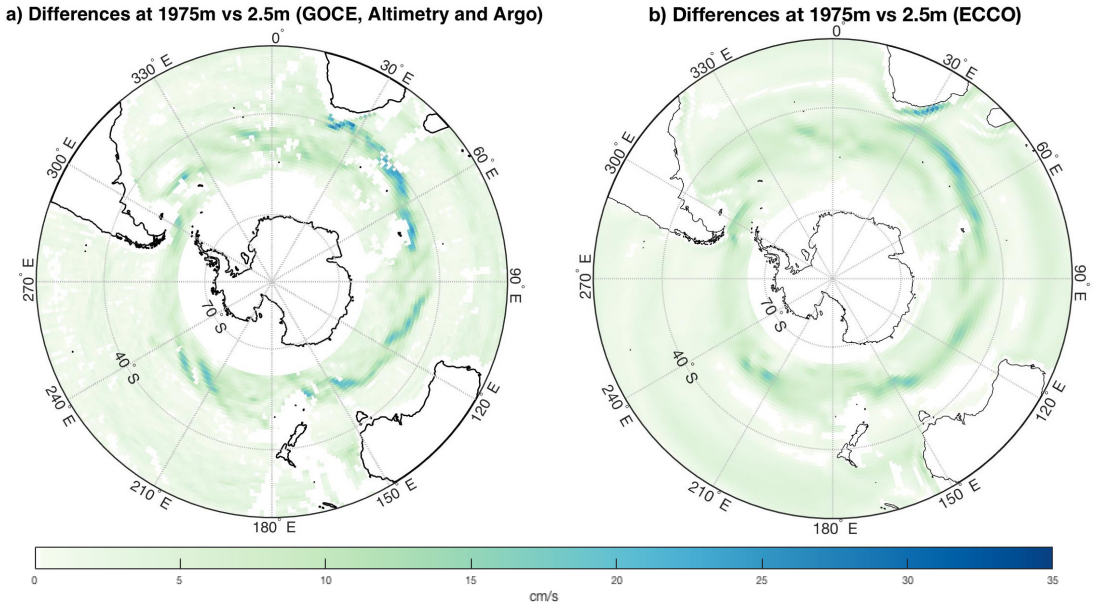

Figure 6. Differences of mean speed from geostrophic currents at 1975 m vs. 2.5 m of depth: (**a**) this study (GOCE, Altimetry and Argo based) ; (**b**) from ECCO model.

For comparison, Figure 7 shows the time series of the zonal geostrophic current speeds at 1000 m depth at two different locations characterized by very different current intensities. The first location is

(40°S, 138°E), south of Australia and north of the subtropical front, where zonal currents are small, and shows a mean zonal speed of 0.1 ± 0.2 cm/s, with standard deviation of 2.4 cm/s. The second location is (51°S, 148°E), south of Tasmania close to the polar front, where the currents are expected to be large. The mean zonal speed there is estimated to be 12 ± 0.8 cm/s with a standard deviation of 8.8 cm/s. The zonal speed at these two locations has also been studied by [14], following a similar methodology but using a GRACE derived geoid. For the overlapping time period (2004–2012), the time series variability is similar to that reported by [14], but intensities obtained by our approach at the second location are considerably larger. That is in agreement with previous studies (e.g., [34–38]) that reported how GOCE geoid enhances the estimate of geostrophic circulation over the GRACE geoid in providing more detailed patterns and higher intensities closer to in-situ observations. The dotted lines are the zonal speed at 1000 m as estimated from the ECCO model, which again under-estimates it.

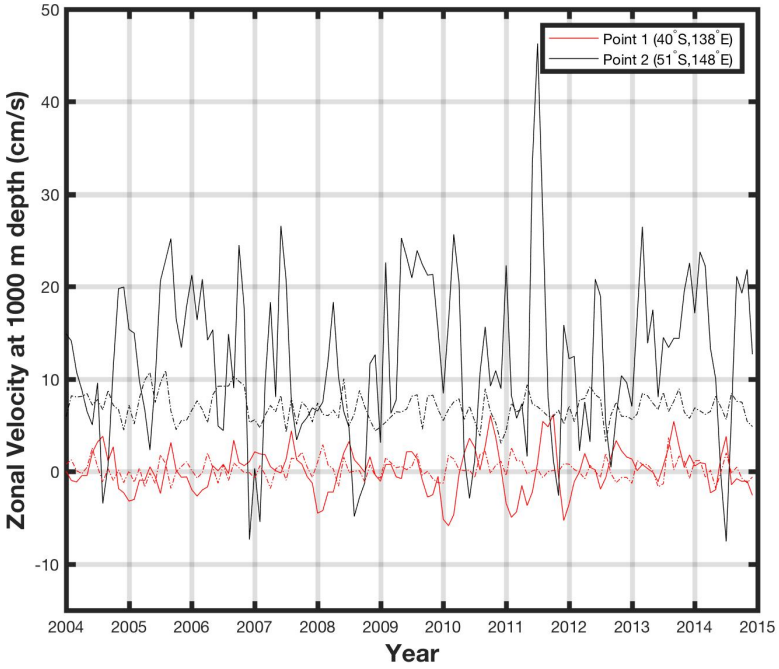

Figure 7. Time series of zonal speed at 1000 m depth at two localities as a function of time (2004–2014): Red curve for (40°S, 138°E) in South Australia (Point1), and black curve for (51°S, 148°E) south of Tasmania (Point 2). Solid lines are our results, dotted lines are those from the ECCO Model.

4.3. Volume Transports

The 3D integrated zonal and meridional VT are evaluated according to Equation 6 (see Section 2), with the limit of integration going from 1975 m depth to the surface. Following [39] we define the barotropic transport as the portion of VT due to a water column moving uniformly as fast as the bottom current, and baroclinic transport as the part of VT with respect to the barotropic transport, so that the geostrophic VT is the sum of the two. The time averaged VT for the period 2004–2014 is shown in Figure 8 in two different ways. Arrows in Figure 8a are the mean VT vectors, while the colored background shows their Euclidean norm, where the color scale is saturated at 80 Sv (maximum values can reach 129 Sv) for better visualization. On the other hand, Figure 8b gives the mean of the monthly VT vector norms map. In this case the maximum values reach 141 Sv, and the color scale saturated at 100 Sv. The 'ACC region' is defined as the grid points in Figure 8b with values above 20 Sv (some isolated points, likely outliers, have been edited out).

As expected, the VT patterns are similar to those from the geostrophic currents. In particular, ACC can be clearly identified as the dominant current. The eastward component is driving the transport, with some alternating north-south departures produced by eddies. In some areas, as in the

south of Africa, the subantarctic and polar fronts can be discerned. The mean of the monthly VT vector norms in 1° grid cell width reaches values from 10.5 Sv at a few points to 141 Sv, with a mean value 35.8 ± 0.5 Sv. On the other hand, the norm of the mean vectors is 29.6 ± 0.4 Sv per 1° grid cell width, from which 22.6 ± 0.3 Sv is of barotropic origin and 7.1 ± 0.1 Sv is baroclinic transport. Hereafter, we will call the Euclidean norm of the mean VT vectors the total VT. Figure 9 shows the time evolution in the ACC region of the zonal, meridional, and total VT, for both the barotropic and the baroclinic components and their sum. Note that these values refer to the VT per 1° grid cell. So, for any section along a meridian, the mean zonal VT at a given time can be estimated multiplying the zonal value at Figure 9 at such time by the number of grid points at the given section. A time average of the volume transport at those sections can be found later in this section. Besides, as the mean number of grid points per meridional section is 10, it can be inferred that the mean VT for this kind of section is 296 Sv. The total VT as shown in Figure 9 is indistinguishable from the zonal component. Approximatively 75% of the mean VT is barotropic, while the remaining 25% is baroclinic. However, the variability of the VT is entirely driven by the barotropic transport. In particular, the VT (and the barotropic component) shows an annual signal of 0.33 ± 0.06 Sv fully driven by the barotropic transport, reaching the maximum on about 8 April. The annual signal explains a 32% of the standard deviation of the signal for total VT. The semiannual signal and the linear trends are not significantly different from zero. Temporally, the total VT and the total barotropic transport show an oscillation with a period of 2–3 years. On the other hand, the mean meridional VT in the ACC (see Figure 9b) shows a mean value of −0.6 ± 0.2 Sv, which means a southward transport. Around 70% of the meridional mean ACC transport is barotropic and 30% is baroclinic, its variability driven by the barotropic transport. None of them display significant annual, semiannual or linear trends, although a decadal oscillation seems to be discernible.

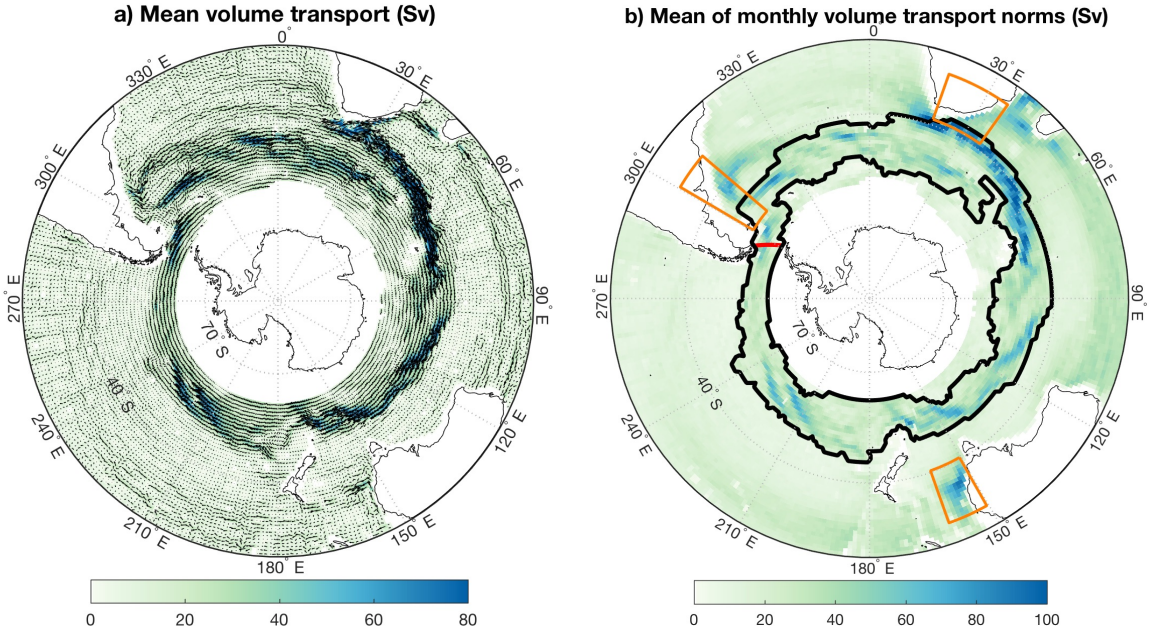

Figure 8. 2004–2014 mean geostrophic volume transport: (**a**) Arrows are the mean vectors, and the color represents their norms. (The color scale is saturated at 80 Sv, maximum values can reach 129 Sv); (**b**) Mean of the monthly vector norms. The ACC region is outlined in black, the Drake Passage in red, and the regions considered for the Agulhas, Brazil-Malvinas and East Australia currents are outlined in orange. The color scale is saturated at 100 Sv, maximum values can reach 141 Sv. Units are Sv.

Of great interest in the ACC is the Drake Passage (red line in Figure 8b), the narrowest part of the current, which is also one of the most studied areas in the Southern Ocean with a large amount of in situ data. The VT in the Drake Passage is estimated by simply adding the VT vectors at the

Drake Passage grid points (red line in Figure 8b, a total of 6 grid cells). Our estimation considering the mean of the monthly VT vector norms is 202.7 Sv, with a standard deviation of 32.4, while considering the total VT (norm) of the mean vector is 185.2 Sv. This estimate is quite a bit larger than those reported in the literature, which range from 134 to 141 Sv (e.g., [5,19,20]), and more recently between 173.3 ± 11 Sv [3] and 175 ± 5 Sv [7]. The differences are apparently reduced when only the zonal component is considered, which shows a mean value of 181.5 Sv with a standard deviation of 43.9 Sv. The origin of this discrepancy is not clear, and will be discussed later. Figure 10a shows the temporal variation of the total VT through the Drake Passage. It shows a big discrepancy from the mean total VT of the ACC (Figure 9); the latter shows an annual signal that is absent in the Drake Passage, whose interannual variability shown by the 12-month running means is not similar either. The total VT at the Drake Passage is quite stable during the period; only a slight increase of around 15 Sv is shown between 2011–2012. Yet the signal varies from year to year; for example, the mean signal is 193 Sv in 2007, and 220 Sv in 2011. In any case, the total VT at Drake Passage is quite stable while considerable variability can be observed in the (dominant) zonal and (relatively small) meridional components (Figure 10a). The meridional component is much smaller at a mean value of 36.5 Sv and a standard deviation of 22.2 Sv. The two components' variability are highly correlated with a (negative) coefficient of −0.86, as can be seen in Figure 10b. They largely add to each other to form a relatively steady total VT. When the total VT is decomposed in the perpendicular and parallel directions of the Drake Passage, the mentioned variability exists only in the parallel direction, which could be interpreted as a small oscillation on the main direction of the total VT.

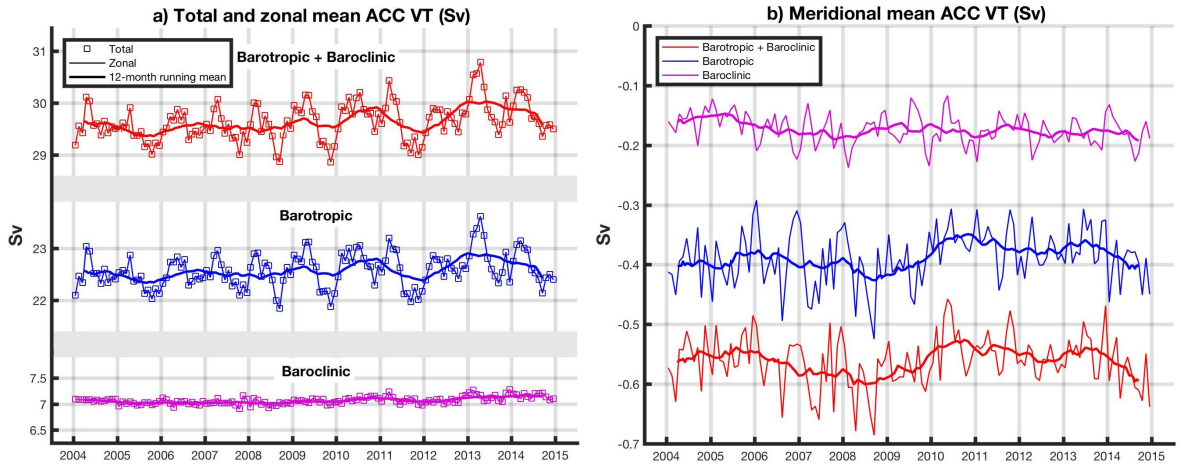

Figure 9. Volume transport in the ACC region per 1° grid cell: (**a**) zonal (thin curves) and total (squares) VT; (**b**) mean meridional (thin curves) VT. Barotropic transport in blue, baroclinic transport in magenta, and their sum (barotropic+baroclinic) in red. Thick curves are 12-months running means. Note that these values refer to the VT per unit cross-section area. Units are Sv.

The barotropic and baroclinic components of the VT at Drake Passage is shown in Figure 10c,d. The former accounts for about 80% of the VT, while the latter accounts for the remaining 20%. As in the ACC, the variability of VT at Drake Passage is entirely related to barotropic transport. Note that the VT and the barotropic transport show similar standard deviations for all components, and a significant correlation coefficient of 0.98. The baroclinic transport shows standard deviations 10 times smaller, and correlation coefficients between 0.3 and 0.4.

Other major current systems apart from the ACC are clearly observed in Figure 8b. Three of them are outlined in the orange box in the map: the Brazil-Malvinas current ([53.5°S, 30.5°S] × [300.5°E, 310.5°E]), the Agulhas current ([38.5°S, 25.5°S] × [19.5°E, 35.5°E]), and the East Australian current [40.5°S, 25.5°S] × [150.5°E, 160.5°E]. In all cases the currents are selected as the grid points with speeds above 20 Sv. The Brazil-Malvinas current shows a mean of the VT vector norms of 39.4 ± 0.7 Sv, and a

total VT of 23.3 ± 0.8 Sv. The Agulhas current shows a mean of the VT vector norms of 60.1 ± 2.6 Sv, and a total VT of 35.5 ± 2.8 Sv. In the southern part of the Agulhas system, near the coast in the region delimited by 31.5°S–32.5°S, and 30.5°E–31.5°E the water flows southward along the coast, and we have a southward meridional transport of 68.9 Sv, which is close to the 69.7 Sv reported in [40] or the 76 Sv in [41]. Note the differences with both approaches: results in Bryden et al. [40] are based on one year data (1995) from an array of six moorings, which are extrapolated to the whole area and integrated from 0 to 2400 m depth, and in Donohue et al. [41] are based on data from only the first half of 1995, while our results combine 11 years of satellite data (not includeding 1995) in 1° × 1° fields integrated from 0 to 1975 m. The East Australian current shows a mean of the VT vector norms of 47.9 ± 1.7 Sv, and a total VT of 13.4 ± 0.8 Sv. In the smaller region located at 27°S from 153.4–155°E a southward transport of 15.8 ± 10.5 Sv above 2000 m was reported by Sloyan et al. [42], based on data from a mooring array between April 2012 and August 2013. Since the time period overlaps with ours, we computed the mean meridional VT for the same region and time period, and we obtain a southward VT of 14.7 ± 7 Sv. The two studies yield very similar VT estimates, which is remarkable keeping in mind the different nature of the data sets. The agreements corroborate that the estimated VT is robust for the Agulhas and East Australian currents.

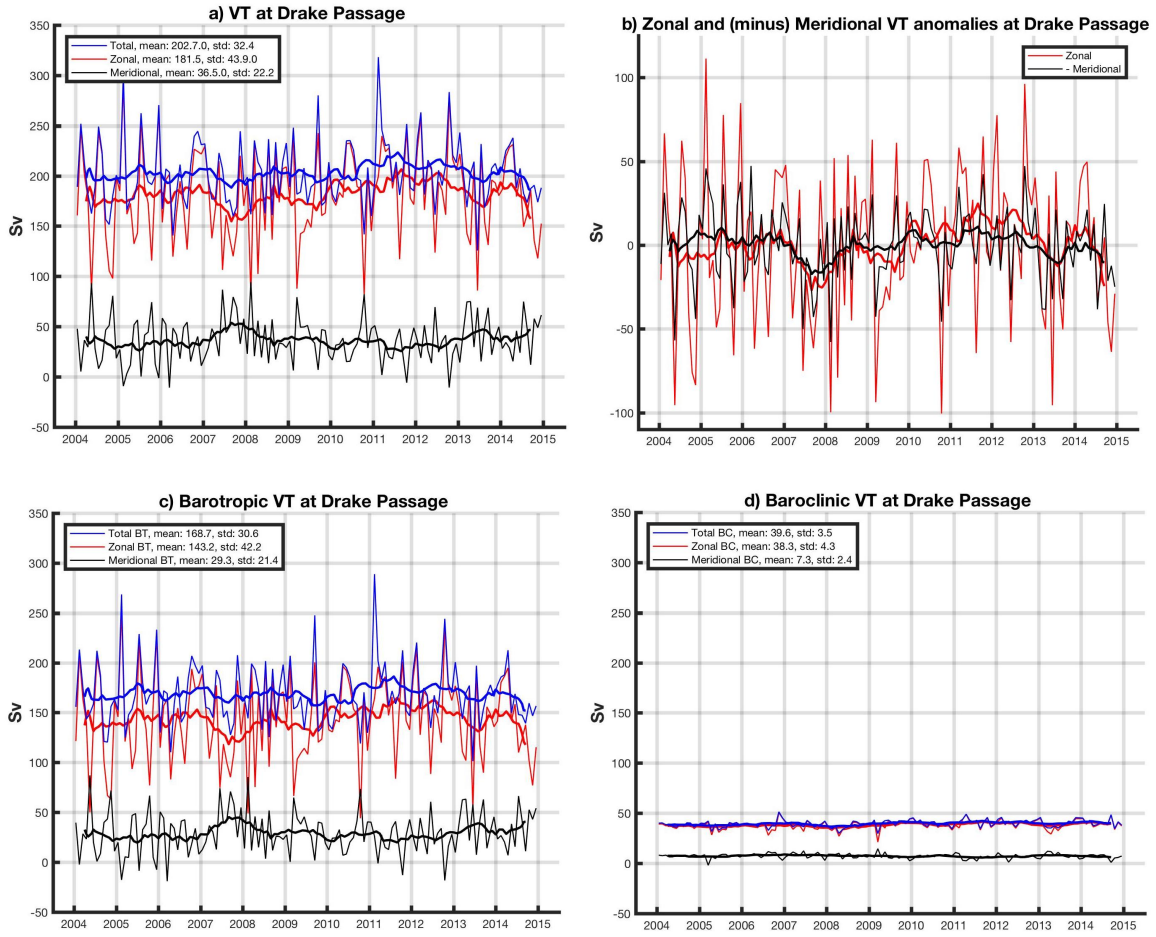

Figure 10. VT at Drake Passage. (**a**) Mean zonal (red), meridional (black), and total VT (blue). (**b**) Anomalies with respect to the mean of zonal and negative meridional signals in (**a**). (**c**) Same as (**a**) but for the barotropic transport. (**d**) Same as (**a**) but for the baroclinic transport. Thick curves are 12-months running means. The sign of the meridional component is reversed to better show its correlation with the zonal component.

In Figure 11, by time averaging and integration latitudinally for the whole region (65°S–20°S, Figure 11a), and the ACC region (Figure 11b), we obtain a longitudinal series of VT and the zonal and meridional components for the Southern Ocean and the ACC. Dotted curves represent the same analysis for barotropic VT. The VT in both regions is clearly dominated by its zonal component, and it is mainly due to barotropic transport. We can clearly identify the three more prominent peaks in the zonal and total VT in Figure 11a with the major local currents, and those roughly delimit the three ocean basins. Around 30°E we find the first peak corresponding to the Agulhas current, from there we are in the Indian Ocean, where we can observe the highest VT until around 115°E. The Australian continent goes from that point to 150°E. In that section the Southern Ocean narrows and the transport remains lower. Then, VT suddenly picks up at the location of the East Australia current around 150°E. From that point we are in the Pacific Ocean until around 285°E, where the Southern Ocean narrows even more at Drake Passage, and that is more or less where the Pacific Ocean connects to the Atlantic Ocean. Around 300°E the peak observed corresponds to the Malvinas current, and the Atlantic Ocean goes from there to 30°E. As expected, at each basin, the VT transport decays from west to east. Thus, the three prominent minima in the zonal and total VT correspond to three choke points of the ACC: the south of Australia between 120°E and 150°E, New Zealand between 170°E and 180°E, and the Drake Passage between 280°E and 300°E. The longitudinal structure of the ACC is similar to that of the whole region, although less pronounced, with the exception of the maximum VT south of Africa, where an almost maximum meridional VT occurs from north to south (Figures 11b and 8a). In any case, it seems that the zonal VT drives the low frequency (in latitude) variability of the total VT, and the meridional VT drives the high frequency (also in latitude). This high variability in the meridional component is due to eddies structures.

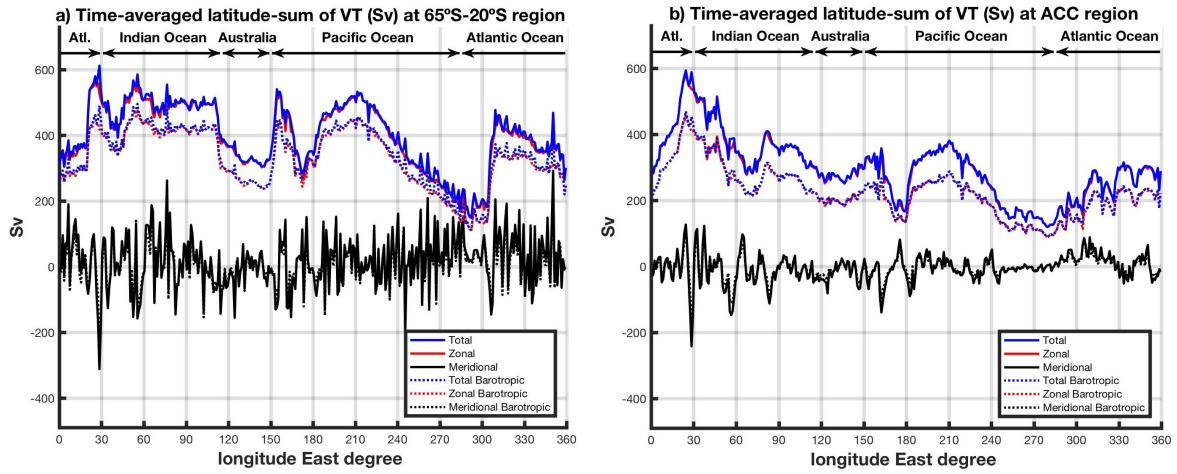

Figure 11. The time-averaged total VT (solid blue curve) and the zonal (solid red curve) and meridional (solid black curve) components of VT. (**a**) Whole region (65°S to 20°S), and (**b**) ACC region (as outlined in Figure 8b). Dotted curves are the same but for barotropic transport.

5. Conclusions

The 3D geostrophic currents and the associated volume transport in the Southern Ocean can be estimated based on data from satellites (altimetric SSH, and a GOCE-based geoid) and Argo floats. The use of an independent geoid from the altimetric SSH is of paramount importance for to better ocean circulations, and the utility of a geoid derived from GOCE is a notable advancement in precision and resolution over those based on the GRACE geoid in previous studies [12–14]. We directly combine the enhanced knowledge of the surface circulation provided by the latest release of GOCE data in combination with altimetry, with in-situ observations of the sub-surface Argo floats to obtain more accurate estimates of the 3D sub-surface geostrophic currents. The results are given as monthly maps

from the surface down to 1975 m depth containing 58 layers. The analyzed region comprises the Southern ocean between 20°S and 65°S, and the time period is 2004–2014. The obtained results clearly depict the currents structure in the Southern Ocean. They are quantitatively compared with previous studies, but it is unable to reproduce the Ross and Weddel Gyres due to the limitation of the Argo data. Surface currents are in remarkably good agreement with those from the drifter observations. Comparisons with output from the ECCO model that also assimilates altimetry SSH and Argo data (among others) but that lacks an independent geoid, evidences that the surface geostrophic currents and their decrease in strength by depths, are greatly underestimated in ECCO.

From the estimated 3D geostrophy we obtain the VT that we analyze for the whole region, and in particular for the ACC, showing quite similar behaviour in terms of variability and components contribution. Global estimates of the VT allow us to analyze the ACC as a whole, which is not possible when studying a section of the ACC as the Drake Passage. For the ACC, the signal shows a mean value for each 1° cell width, depending on the method used, of 29.6 (the norm of mean VT) or 35.8 Sv (the mean of VT norms). The baroclinic and barotropic components of the VT are such that 75% of the total transport is barotropic which supports the importance of an independent precise geoid in its determination. Nevertheless, in this study we show the dominance of the barotropic component for the ACC which does not necessary hold in other current systems. The ACC VT presents an annual signal with 0.33 ± 0.06 Sv amplitude that peaks in early April ($97° \pm 11°$), and no significant semi-annual signals or linear trend. The annual signal is of barotropic origin, while the baroclinic annual signal is essentially absent. At Drake Passage, our mean geostrophic VT estimate is 181 Sv for the zonal component, 185 Sv for the norm of the time averaged VT vector, and 202 Sv for the mean of the norms of the monthly VT. These estimates are quite a bit larger than the usual mean values reported in the literature. The methodology and data used being different, assessing possible systematic errors in the VT estimation awaits further research. However, the agreement observed in the Agulhas and the East Australia currents suggests that an overestimation, if it existed, would not have a uniform effect everywhere. Griesel et al. [43] evaluated four different MDT products for the ACC transport, that make use of GRACE satellite gravity for the geoid. They concluded that they all imply an unrealistic lack of mass conservation, which would lead to an overestimation for the ACC transport. As such, the effect of accounting for an ocean mass balance constraint requires further research. Understanding these discrepancies will help to improve the future methodologies. The total VT at the Drake Passage is relatively stable during the studied period, unlike its zonal and meridional components that show variabilities that cancel each other in the total VT, implying that the transport vector oscillates around its mean direction, remaining quasi constant in magnitude.

In summary, the combination of altimetry, space gravimetry missions, and in situ Argo measurements, which are in a state of maturity, has confirmed their capability to yield realistic geostrophic current and VT estimates up to 1975 m depth. This new approach enables the possibility of new studies in oceanography at global scales.

Author Contributions: M.I.V. conceived and designed the study. M.I.V. and D.G.-G. processed and analyzed the data. M.D.S. processed all data to obtain the 3D geostrophy and VT under the supervision of M.I.V. and B.F.C. in an earlier approach of the work. All authors were involved in the analysis of the results and contributed to the discussion of results and the preparation of the manuscript.

Funding: This research was funded by Taiwan MoST grant number106-2116-M-001-013.

Acknowledgments: We thank the three anonymous reviewers whose constructive comments/suggestions helped improve and clarify this manuscript. We acknowledge the support of all data providers: ESA in the frame of the CCI Sea Level Project for Altimetry data; DTU SPACE from the Danish National Space Center for MDT and MSS products; SCRIPPS for Roemmich and Gilson Temperature and Salinity profiles from ARGO data; Global Drifter Program for the near-surface geostrophic currents from drifter buoys; LEGOS and CERSAT for the Ekman Surface Currents. M.D.S. is supported by the phD grant UAFPU2014-5884 from the University of Alicante.

Conflicts of Interest: The authors declare no conflict of interest.

References

1. Richardson, P.L. Worldwide ship drift distributions identify missing data. *J. Geophys. Res.* **1989**, *94*, 6169–6176. [CrossRef]
2. Whitworth, T.; Peterson, R.G. Volume Transport of the Antarctic Circumpolar Current from Bottom Pressure Measurements. *Am. Meteorol. Soc.* **1984**, *15*, 810–816. [CrossRef]
3. Donohue, K.A.; Tracey, K.L.; Watts, D.R.; Chidichimo, M.P.; Chereskin, T.K. Mean Antarctic Circumpolar Current transport measured in Drake Passage. *Geophys. Res. Lett.* **2016**, *43*, 11760–11767. [CrossRef]
4. Frankignoul, C.; Bonjean, F.; Reverdin, G. Interannual variability of surface currents in the tropical Pacific during 1987–1993. *J. Geophys. Res.* **1996**, *101*, 3629–3647. [CrossRef]
5. Cunningham, S.A.; Alderson, S.G.; King, B.A.; Brandon, M.A. Transport and variability of the Antarctic Circumpolar Current in Drake Passage. *J. Geophys. Res.* **2003**, *108*, 8084. [CrossRef]
6. Firing, Y.; Chereskin, T.K.; Mazloff, M.R. Vertical structure and transport of the Antarctic Circumpolar Current in Drake Passage from direct velocity measurements. *J. Geophys. Res.* **2011**, *116*, C08015. [CrossRef]
7. Colin de Verdière, A.; Ollitrault, M. A direct determination of the World Ocean barotropic circulation. *J. Phys. Oceanogr.* **2016**, *46*, 255–273. [CrossRef]
8. Wunsch, C.; Gaposchkin, E.M. On using satellite altimetry to determine the general circulation of the oceans with application to geoid improvement. *Rev. Geophys.* **1980**, *18*, 725–745. [CrossRef]
9. Fu, L.L.; Cazenave, A. (Eds.) *Satellite Altimetry and Earth Science*; Academic Press: New York, NY, USA, 2001; p. 463.
10. Roemmich, D.; Owens, W.B. The Argo Project: Global ocean observations for the understanding and prediction of climate variability. *Oceanography* **2000**, *13*, 45–50. [CrossRef]
11. Rummel, R.; Balmino, G.; Johannessen, J.; Visser, P.; Woodworth, P. Dedicated gravity field missions—Principles and aims. *J. Geodyn.* **2002**, *33*, 3–20. [CrossRef]
12. Cadden, D.D.H.; Subrahmanyam, B.; Chambers, D.P.; Murty, V.S.N. Surface and subsurface geostrophic current variability in the Indian Ocean from altimetry. *Mar. Geod.* **2009**, *32*, 19–29. [CrossRef]
13. Mulet, S.; Rio, M.H.; Mignot, A.; Guineut, S.; Morrow, R. A new estimate of the global 3D geostrophic ocean circulation based on satellite data and in-situ measurements. *Deep Sea Res. II* **2012**, *77–80*, 70–81. [CrossRef]
14. Kosempa, M.; Chambers, D.P. Southern Ocean Velocity and Geostrophic transport fields estimated combining Jason altimetry and ARGO data. *J. Geophys. Res. Oceans* **2014**, *119*, 4761–4776. [CrossRef]
15. Carter, L.; McCave, I.N.; Williams, M.J.M. Circulation and water masses of the Southern Ocean: A review. *Dev. Earth Environ. Sci.* **2008**, *8*, 85–114. [CrossRef]
16. Rintoul, S.R.; Hughes, C.W.; Olbers, A. The Antarctic Circumpolar Current system. In *Ocean Circulation and Climate: Observing and Modelling the Global Ocean*; Siedler, G., Church, J., Gould, J., Eds.; International Geophysics 77; Academic Press: New York, NY, USA, 2001; pp. 271–302, ISBN 978-0-12-641351-9.
17. Rintoul, S.R.; Sokolov, S. Baroclinic transport variability of the Antarctic Circumpolar Current south of Australia (WOCE repeat section SR3). *J. Geophys. Res.* **2001**, *106*, 2815–2832. [CrossRef]
18. Rintoul, S.R.; Sokolov, S.; Church, J. A 6 year record of baroclinic transport variability of the Antarctic Circumpolar Current at 140° E derived from expendable bathythermograph and altimeter measurements. *J. Geophys. Res.* **2002**, *107*, 3155. [CrossRef]
19. Ganachaud, A.; Wunsch, C. Improved estimates of global ocean circulation, heat transport and mixing from hydrographic data. *Nature* **2000**, *408*, 453–457. [CrossRef] [PubMed]
20. Koenig, Z.; Provost, C.; Ferrari, R.; Sennéchael, N.; Rio, M.H. Volume transport of the Antarctic Circumpolar Current: Production and validation of a 20 year long time series obtained from in situ and satellite observations. *J. Geophys. Res. Oceans* **2014**, *119*, 5407–5433. [CrossRef]
21. McDougall, T.J.; Barker, P.M. Getting started with TEOS-10 and the Gibbs Seawater (GSW) Oceanographic 423 Toolbox, version 3.0 (R2010a). *SCOR/IAPSO WG* **2011**, *127*, 1–28; ISBN 978-0-646-55621-5.
22. Ablain, M.; Cazenave, A.; Larnicol, G.; Balmaseda, M.; Cipollini, P.; Faugére, Y.; Fernandes, M.J.; Henry, O.; Johannessen, J.A.; Knudsen, P.; et al. Improved sea level record over the satellite altimetry era (1993–2010) from the Climate Change Initiative project. *Ocean Sci.* **2015**, *11*, 67–82. [CrossRef]
23. Andersen, O.; Knudsen, P.; Stenseng, L. The DTU13 MSS (Mean Sea Surface) and MDT (Mean Dynamic Topography) from 20 years of Satellite Altimetry. In *IAG Symposia*; Springer: Cham, Switzerlands, 2015; doi:10.1007/1345_2015_182.

24. Förste, C.; Bruinsma, S.; Shako, R.; Marty, J.-C.; Flechtner, F.; Abrikosov, O.; Dahle, C.; Lemoine, J.-M.; Neumayer, K.H.; Biancale, R.; et al. EIGEN-6—A new combined global gravity field model including GOCE data from the collaboration of GFZ-Potsdam and GRGS-Toulouse. In Proceedings of the EGU General Assembly, Vienna, Austria, 3–8 April 2011.
25. Roemmich, D.; Gilson, J. The 2004–2008 mean and annual cycle of temperature, salinity, and steric height in the global ocean from the Argo Program. *Prog. Oceanogr.* **2009**, *82*, 81–100. [CrossRef]
26. Fukumori, I.; Wang, O.; Fenty, I.; Forget, G.; Heimbach, P.; Ponte, R.M. ECCO Version 4 Release 3. 2017, Available online: ftp://ecco.jpl.nasa.gov/Version4/Release3/doc/v4r3_estimation_synopsis.pdf (accessed on April 2018).
27. Forget, G.; Campin, J.-M.; Heimbach, P.; Hill, C.N.; Ponte, R.M.; Wunsch, C. ECCO version 4: An integrated framework for non-linear inverse modeling and global ocean state estimation. *Geosci. Model Dev.* **2015**, *8*, 3071–3104. [CrossRef]
28. Sudre, J.; Maes, C.; Garçon, V.C. On the global estimates of geostrophic and Ekman surface currents. *Limnol. Oceanogr. Fluids Environ.* **2013**, *3*, 1–20. [CrossRef]
29. Laurindo, L.; Mariano, A.; Lumpkin, R. An improved near-surface velocity climatology for the global ocean from drifter observations. *Deep-Sea Res. I* **2017**, *124*, 73–92. [CrossRef]
30. Laurindo, L. On the Air-Sea Exchange of Mechanical Energy: A Meso to Large-Scale Assessment Using Concurrent Drifter and Satellite Observations. Ph.D. Dissertation, University of Miami, Coral Gables, FL, USA, **2018**.
31. Zhang, Z.-Z.; Chao, B.F.; Lu, Y.; Hsu, H.-T. An effective filtering for GRACE time-variable gravity: Fan filter. *Geophys. Res. Lett.* **2009**, *36*, L17311. [CrossRef]
32. Johnson, G.C.; Bryden, H.L. On the size of the Antarctic Circumpolar Current. *Deep-Sea Res.* **1989**, *36*, 39–53. [CrossRef]
33. Kundu, P.J. Ekman Veering Observed near the Ocean Bottom. *J. Phys. Oceanoghrapy* **1975**, *6*, 238–242. [CrossRef]
34. Bingham, R.J.; Knudsen, P.; Andersen, O.; Pail, R. An initial estimate of the North Atlantic steady state geostrophic circulation from GOCE. *Geophys. Res. Lett.* **2011**, *38*, L01606. [CrossRef]
35. Feng, G.; Jin, S.; Sanchez-Reales, J.M. Antarctic circumpolar current from satellite gravimetric models ITG-GRACE2010, GOCE-TIM3 and satellite altimetry. *J. Geodyn.* **2013**, *72*, 72–80. [CrossRef]
36. Knudsen, P.; Bingham, R.; Andersen, O.; Rio, M.H. A global mean dynamic topography and ocean circulation estimation using a preliminary GOCE gravity model. *J. Geod.* **2011**, *85*. [CrossRef]
37. Sánchez-Reales, J.M.; Vigo, M.I.; Jin, S.G.; Chao, B.F. Global Surface Geostrophic Currents from Satellite Altimetry and GOCE. In Proceedings of the 4th International GOCE User Workshop, Munich, Germany, 31 March–1 April 2011, ESA SP-696.
38. Sánchez-Reales, J.M.; Vigo, M.I.; Jin, S.G.; Chao, B.F. Global Surface Geostrophic Currents Derived from Satellite Altimetry and GOCE Geoid. *Mar. Geod.* **2012**, *35*, 175–189. [CrossRef]
39. Fofonoff, N.P. Dynamics of ocean currents. In *The Sea. Volume 1: Physical Oceanography*; Wiley-Interscience: Hoboken, NJ, USA, 1962; pp. 323–395.
40. Briden, H.L.; Beal, L.M.; Duncan, L.M. Structure and Transport of the Agulhas Current ant its temporal variability. *J. Oceanogr.* **2005**, *61*, 479–492. [CrossRef]
41. Donohue, K.A.; Firing, E.; Beal, L. Comparison of three velocity sections of the Agulhas Current and Agulhas Undercurrent. *J. Geophys. Res.* **2000**, *105*, 28585–28593. [CrossRef]
42. Sloyan, B.M.; Ridgway, K.R.; Cowley, R. The East Australian Current and Property Transport at 27°S from 2012 to 2013. *J. Phys. Oceanogr.* **2016**, *46*. [CrossRef]
43. Griesel, A.; Mazloff, M.R.; Gille, S.T. Mean dynamic topography in the Southern Ocean: Evaluating Antarctic Circumpolar Current transport. *J. Geophys. Res.* **2011**, *117*, C01020. [CrossRef]